

## ACCURATE ASTROMETRY AND PHOTOMETRY OF SATURATED AND CORONAGRAPHIC POINT SPREAD FUNCTIONS

CHRISTIAN MAROIS,<sup>1</sup> DAVID LAFRENIÈRE,<sup>2</sup> BRUCE MACINTOSH,<sup>1</sup> AND RENÉ DOYON<sup>2</sup>

*Received 2006 February 6; accepted 2006 April 11*

### ABSTRACT

Accurate astrometry and photometry of saturated and coronagraphic point-spread functions (PSFs) are fundamental to both ground- and space-based high-contrast imaging projects. For ground-based adaptive optics (AO) imaging, differential atmospheric refraction and flexure introduce a small drift of the PSF with time, and seeing and sky transmission variations modify the PSF flux distribution. For space-based imaging, vibrations, thermal fluctuations, and pointing jitters can modify the PSF core position and flux. These effects need to be corrected to properly combine the images and obtain optimal signal-to-noise ratios, accurate relative astrometry, and photometry of detected objects, as well as precise detection limits. Usually, one can easily correct for these effects by using the PSF core, but this is impossible when high dynamic range observing techniques are used, such as coronagraphy with a nontransmissive occulting mask or if the stellar PSF core is saturated. We present a new technique that can solve these issues by using off-axis satellite PSFs produced by a periodic amplitude or phase mask conjugated to a pupil plane. We show that these satellite PSFs track precisely the PSF position, its Strehl ratio, and its intensity, and can thus be used to register and to flux-normalize the PSF. A laboratory experiment is also presented to validate the theory. This approach can be easily implemented in existing AO instruments and should be considered for future extreme AO coronagraph instruments and in high-contrast imaging space observatories.

*Subject headings:* instrumentation: adaptive optics — planetary systems — stars: imaging

### 1. INTRODUCTION

Accurate astrometry and photometry of saturated and coronagraphic point-spread functions (PSFs) are fundamental to both ground- and space-based high-contrast imaging of brown dwarfs and exoplanets. Achieving precise astrometry is important to minimize the time required to confirm via proper-motion analysis that two objects are gravitationally bound, i.e., that a newly found companion is not a background object, and to better constrain its orbit. Precise photometry is essential to better understand the companion's physical characteristics. For ground-based adaptive optics (AO) imaging, both standard observing techniques and more specialized observing methods, such as simultaneous spectral differential imaging (Racine et al. 1999; Marois et al. 2000, 2005; Sparks & Ford 2002; Biller et al. 2004; Marois 2004), angular differential imaging (Marois 2004; Liu 2004; Marois et al. 2006), and coronagraphy (Lyot 1932), generally require the acquisition of a long sequence of images. The object air mass, the telescope orientation, and the observing conditions (seeing and sky transmission) change during the sequence, producing PSF flux and Strehl ratio variations over time. The PSF is also slowly moving and evolving due to flexure and differential atmospheric refraction if a near-infrared camera is used while operating the AO wave front sensor in the visible. Space-based imaging is also affected by similar problems from vibrations, thermal fluctuations, and pointing jitters. If not corrected, these effects bias the relative photometry and astrometry of detected sources and the estimated sensitivity limits. To obtain the optimal signal-to-noise ratio (S/N) and precise astrometry and photometry after the combination of all acquired images, each individual image needs to be accurately registered and flux normalized.

Standard techniques to properly register a PSF and to estimate the relative astrometry and photometry generally require the PSF core. If the PSF core is saturated to improve observing efficiency or if a nontransmissive focal plane occulter is used, the PSF core is not visible and other techniques need to be applied. If available, an off-axis sharp ghost image can be used to register the PSF and estimate its core position, but the possibility of a non-common motion between the ghost and the PSF makes the registering uncertain.

The usual technique for estimating sensitivity limits (or a source relative intensity) when the PSF core is saturated or occulted is to compare the noise in the combined image (or a source peak intensity) to the peak intensity of an unsaturated/unocculted PSF acquired before and/or after the saturated/occulted image sequence. Such estimates can be biased by the short exposure time and the generally small number of unsaturated/unocculted images. Furthermore, the observing conditions of the unsaturated/unocculted images can be significantly different from those of the saturated/occulted image sequence.

To obtain the highest S/N in the combined image, one would want ideally to normalize the images such that any point source, after image registration, has the same number of counts per FWHM in each image. The images would then be weighted by the inverse square of their noise and combined.

A simple solution to these astrometric and photometric problems exists. A periodic phase or amplitude mask can be introduced at a pupil plane to produce fainter off-axis copies of the primary PSF. The position and relative intensity of these satellite PSFs are mainly fixed by the mask amplitude and spatial periodicity. These satellite PSFs track precisely the PSF core position, as well as its intensity variations. They can thus be used for accurate astrometry and photometry. Here this technique is first analyzed using a simple analytical model and numerical simulations. The technique is then validated using a laboratory experiment. A technique similar to the one presented in this paper has been independently developed by Sivaramakrishnan & Oppenheimer (2006).

<sup>1</sup> Institute of Geophysics and Planetary Physics, L-413, Lawrence Livermore National Laboratory, 7000 East Avenue, Livermore, CA 94550.

<sup>2</sup> Département de physique et Observatoire du Mont Mégantic, Université de Montréal, C.P. 6128, Succursale A, Montréal, QC H3C 3J7, Canada.

## 2. NONCORONAGRAPHIC PSFs

The effect of a pupil-plane conjugated aberration can be estimated using a far-field approximation. The intensity  $I(\eta, \xi)$ , where  $\eta$  and  $\xi$  are coordinates in the focal plane, of the PSF is simply the Fourier transform (FT) of the complex electric field (Schroeder 1987) at the pupil:

$$I(\eta, \xi) = \left| \text{FT} \left[ A(x, y) e^{i[\phi(x, y)]} \right] \right|^2 \equiv |F_a|^2 \equiv I_a, \quad (1)$$

where  $A$  is the wave front amplitude, equal to 1 inside the pupil and zero elsewhere, and  $\phi$  is its phase, having a noise rms  $\sigma$  inside the pupil. Both  $A$  and  $\phi$  are expressed in coordinates  $x$  and  $y$  in the pupil and are real functions. The phase  $\phi$  has zero mean. The functions  $I_a$  and  $F_a$  are, respectively, the aberrated PSF intensity and its complex focal plane electric field. The next two subsections study the effect of adding a specific phase or amplitude pupil-plane mask to the aberrated wave front. It is assumed in the following analysis that  $\phi(x, y)$  is small (space based or AO imaging), producing diffraction-limited images.

### 2.1. Pupil-Plane Periodic Phase Mask

If a phase aberration  $\phi_{\text{mask}}$  having an FT equal to  $\Phi_{\text{mask}}$  and a standard deviation  $\sigma_{\text{mask}}$  is introduced on the wave front at a pupil plane, the modified PSF intensity can be deduced from equation (1). The aberration  $\phi$  is simply replaced by  $\phi + \phi_{\text{mask}}$ , and the following expression is found:

$$I(\eta, \xi) = \left| \text{FT} \left[ A(x, y) e^{i[\phi(x, y) + \phi_{\text{mask}}(x, y)]} \right] \right|^2. \quad (2)$$

Separating the effect of the mask, we find

$$I(\eta, \xi) = \left| \text{FT} \left( \left[ A(x, y) e^{i[\phi(x, y)]} \right] \left[ e^{i[\phi_{\text{mask}}(x, y)]} \right] \right) \right|^2. \quad (3)$$

Following the work of Bloemhof et al. (2001), Sivaramakrishnan et al. (2002), and Perrin et al. (2003), assuming  $\phi_{\text{mask}}$  is small, the complex exponential of  $\phi_{\text{mask}}$  can be expanded using a Taylor approximation to find

$$I(\eta, \xi) \cong \left| \text{FT} \left( \left[ A(x, y) e^{i[\phi(x, y)]} \right] \left[ 1 + i\phi_{\text{mask}} - \frac{\phi_{\text{mask}}^2}{2} + \dots \right] \right) \right|^2. \quad (4)$$

We can then use the equation derived in Perrin et al. (2003) to find

$$I(\eta, \xi) \cong \sum_{n=0}^{\infty} p_n, \quad (5)$$

$$p_n = i^n \sum_{k=0}^n \frac{(-1)^{n-k}}{k!(n-k)!} (F_a \star^k \Phi_{\text{mask}}) (F_a^* \star^{n-k} \Phi_{\text{mask}}^*), \quad (6)$$

where  $\star^n$  is for an  $n$ -fold convolution operator, e.g.,  $x \star^3 y = x \star y \star y \star y$ . If the phase mask is chosen to be a periodic function,  $\Phi_{\text{mask}}$  is sharply peaked at symmetric locations. The terms proportional to  $F_a \star^i \Phi_{\text{mask}}$  thus simply add replicas of  $F_a$  at each peak of  $\Phi_{\text{mask}}$  and at integer multiples of these peaks for multiple convolutions. Keeping only terms up to the second order, we find

$$I(\eta, \xi) \cong I_a + 2\Re[F_a^* (F_a \star \Phi_{\text{mask}})] - \Re[F_a^* (F_a \star \Phi_{\text{mask}} \star \Phi_{\text{mask}})], \quad (7)$$

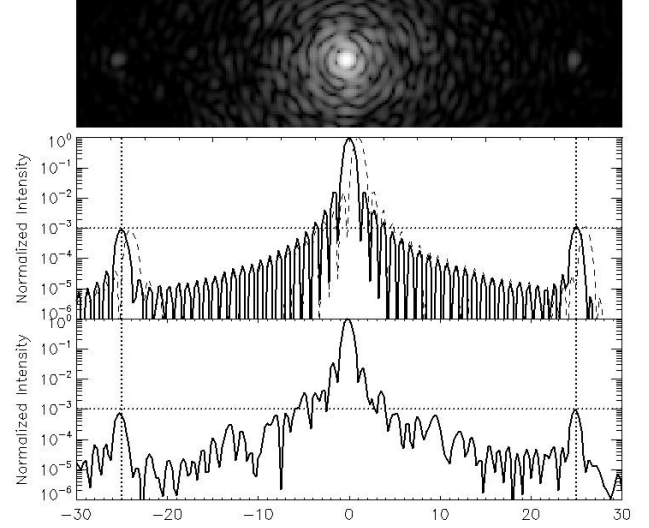


FIG. 1.—*Middle panel*: Simulated monochromatic PSF with added sine wave phase mask (solid line). The dashed line shows the same simulation with an added tilt to show that the satellite PSFs track the PSF core position. *Top and bottom*: Same simulation with an added 150 nm rms phase aberration. The dotted lines show the satellite PSFs' expected positions and intensities. The top panel is shown on a logarithmic scale.

where the symbols  $\Im$  and  $\Re$  denote, respectively, the imaginary and real parts. Both the second and third terms are interference effects between the aberrated PSF and  $\Phi_{\text{mask}}$ . For the replicas to be greater than  $I_a$  at the same separation,  $\sigma_{\text{mask}}$  needs to be larger than the noise component of  $\sigma$  at the spatial frequency corresponding to the mask periodicity. Noting that  $F_a$  sharply drops with angular separation, since both the second and third terms are multiplied by  $F_a$  and since  $\Phi_{\text{mask}}$  is selected to be brighter than  $F_a$  ( $\Phi_{\text{mask}} \gg F_a$  at  $\Phi_{\text{mask}}$  maxima), both terms can be neglected when compared to the fourth one. In that case, we find that the PSF intensity evolution due to the phase mask is simply

$$I(\eta, \xi) - I_a \cong |F_a \star \Phi_{\text{mask}}|^2. \quad (8)$$

Since  $F_a$  is the aberrated PSF electric field and the periodic phase mask produces replicas of the aberrated PSF, we call these satellite PSFs. Since the satellite PSFs are produced by a convolution of the aberrated PSF, they track the PSF core position and intensity variations. The intensity and location of the satellite PSFs are, respectively, set only by the amplitude and periodicity of the phase mask, and they are thus insensitive, to first order, to a mask offset. A discussion of the neglected terms and their effects on the astrometric and photometric precision can be found in § 4.

If we assume that the phase mask is a sine wave, two satellite PSFs will be produced at an angular separation equal to the number of cycles per pupil in  $\lambda/D$  units and with a relative intensity equal to  $\sigma_{\text{mask}}^2/2$ . Figure 1 shows an unaberrated  $1.6 \mu\text{m}$  monochromatic PSF with a 11 nm amplitude sine wave phase mask having 25 cycles per pupil, as well as a PSF having the same sine wave phase mask but with a 150 nm rms phase aberration. The aberration power spectral density (PSD) follows a power law of index  $-2.6$ . It is expected that satellite PSFs will be 1000 times fainter than the PSF and located at  $25 \lambda/D$ . PSFs are simulated with a 256 pixel diameter circular pupil inside a  $1024 \times 1024$  pixel image, producing a PSF having 4 pixels per  $\lambda/D$ . The satellite PSFs are clearly at their predicted location; they have the

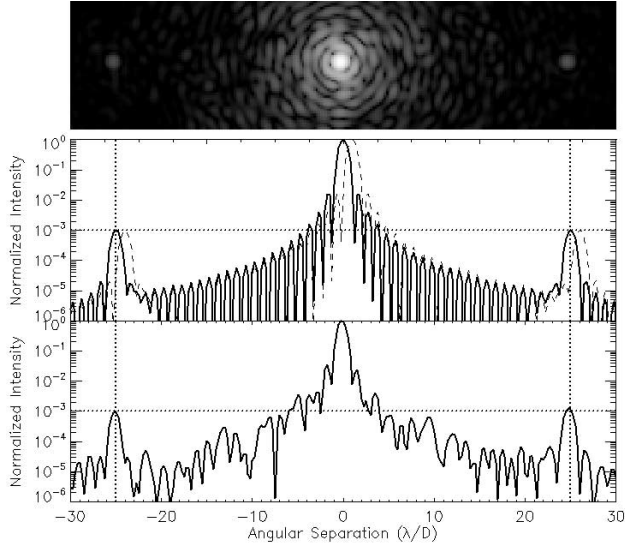


FIG. 2.—Same as Fig. 1, but for an added amplitude sine wave mask.

estimated relative intensity, and they track the PSF core position, Strehl ratio, and its intensity. These satellite PSFs can thus be used for registration and photometric calibration (see § 5).

### 2.2. Pupil-Plane Periodic Amplitude Mask

A similar analysis can be done for a pupil-plane conjugated amplitude mask. Introducing an amplitude mask  $\epsilon_{\text{mask}}$  having an FT equal to  $E_{\text{mask}}$  and a standard deviation  $\sigma_{\text{mask}}$  on the wave front conjugated to the pupil plane modifies equation (1) as follows:

$$I(\eta, \xi) = \left| \text{FT} \left( [A + A\epsilon] e^{i[\phi(x,y)]} \right) \right|^2. \quad (9)$$

Reorganizing this equation, we find

$$I(\eta, \xi) = \left[ \text{FT} \left( A e^{i[\phi(x,y)]} \right) + \text{FT} \left( [A\epsilon] e^{i[\phi(x,y)]} \right) \right] \times \left[ \text{FT} \left( A e^{i[\phi(x,y)]} \right) + \text{FT} \left( [A\epsilon] e^{i[\phi(x,y)]} \right) \right]^*. \quad (10)$$

Knowing that the FT of a multiplication is the convolution of the two FTs, we find

$$I(\eta, \xi) = I_a + 2\Re[F_a(F_a^* \star E^*)] + |F_a \star E|^2. \quad (11)$$

Following the argument of § 2.1, the second term can be neglected, and we find the modified PSF intensity to be

$$I(\eta, \xi) - I_a \cong |F_a \star E|^2. \quad (12)$$

The satellite PSFs are thus again copies of the primary aberrated PSF. See § 4 for a discussion of the neglected term and its effect on the astrometric and photometric precision.

If the amplitude mask is a sine wave, the satellite PSFs have a relative intensity equal to  $\sigma_{\text{mask}}^2/2$  and their separation is equal to the number of cycles per pupil in  $\lambda/D$  units. Figure 2 shows an unaberrated  $1.6 \mu\text{m}$  monochromatic PSF with a 4% amplitude sine wave transmission mask having 25 cycles per pupil, as well as an aberrated PSF with the same sine wave mask but with 150 nm rms phase aberration, as in § 2.1. It is expected that satellite PSFs will be at  $25 \lambda/D$  separation and 1000 times fainter than the PSF. Similarly to what has been found for a phase mask, the satellite PSFs are at their predicted location, they have the estimated relative intensity, and they track the PSF core position and its intensity.

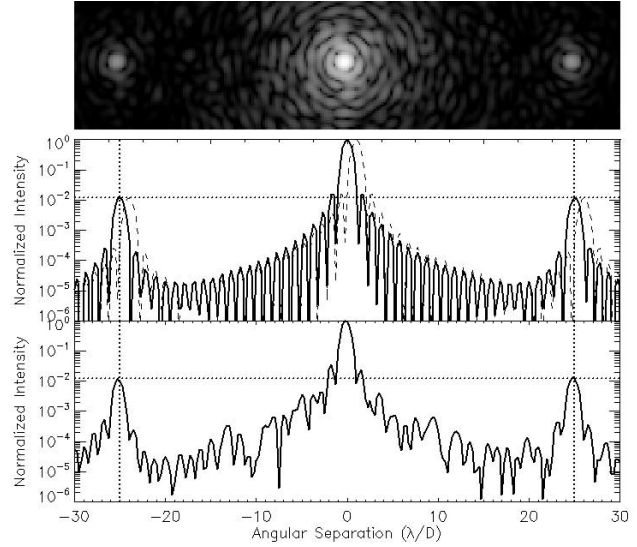


FIG. 3.—Same as Fig. 1, but for an added transmissive amplitude grating. This figure shows the first two bright satellite PSFs. Numerous fainter satellite PSFs exist at wider separation.

Instead of a sine wave amplitude mask, another option is to simply use a transmission amplitude grating consisting of wires to mask a periodic section of the pupil. In that case, equation (12) is still valid, and the satellite PSFs will be the convolution of the wire grid FT with the aberrated PSF. The wire grid can be treated as a multislit Young experiment and the satellite PSFs' intensity function  $I^s$  is thus simply (Hecht 1998)

$$I^s(\theta) = I_0^s \left( \frac{\sin \beta}{\beta} \right)^2 \left( \frac{\sin N\alpha}{\sin \alpha} \right)^2, \quad (13)$$

where  $\theta$  is the angular separation along the satellite PSFs' axis,  $I_0^s$  is the intensity at  $\theta = 0$ ,  $N$  is the number of wires across the pupil, and  $\beta$  and  $\alpha$ , respectively, are equal to  $(kb/2)\sin \theta$  and  $(ka/2)\sin \theta$ . The constant  $k$  is the propagation number ( $2\pi/\lambda$ ), and the values  $a$  and  $b$  are, respectively, the wire spacing and thickness. The first parenthesis in equation (13) is the intensity envelope produced by the diffraction of a single wire (sinc function having  $\sim \lambda/b$  FWHM), while the second parenthesis is the intensity modulation from the interference of diffracted light from all wires. Satellite PSFs (local maxima) appear at  $m\lambda/a$  separations, where  $m$  is an integer. In contrast to the phase and amplitude sine wave masks that show two satellite PSFs, the transmission amplitude grating produces numerous satellite PSFs. The relative intensity, at  $\theta = 0$ , of the satellite PSFs is equal to the square of the ratio of the area masked by the grating over that in the unobscured pupil region:

$$\frac{I_0^s}{I_0} = \left[ \frac{\int_{\text{pupil}} (A\epsilon) dx dy}{\int_{\text{pupil}} (A + A\epsilon) dx dy} \right]^2, \quad (14)$$

where  $I_0$  is the aberrated PSF peak intensity. For a uniform pupil having numerous wires, the circular shape of the pupil can be neglected and the intensity ratio is approximated by

$$\frac{I_0^s}{I_0} \cong \left( \frac{b}{a-b} \right)^2. \quad (15)$$

If  $a \gg b$ , the ratio is simply  $(b/a)^2$ .

Figure 3 shows an unaberrated  $1.6\ \mu\text{m}$  monochromatic PSF simulation with a grating having 25 wires across the pupil, each of width equal to  $1/250$  of the pupil diameter, as well as an aberrated PSF (150 nm rms phase aberration) with the same grating (for these simulations, the pupil diameter is 250 pixels and the image has  $1000 \times 1000$  pixels). It is expected that the first satellite PSFs will be at  $25\ \lambda/D$  separation and 81 times fainter than the PSF. The added satellite PSFs are at their predicted location; they have the estimated relative intensity, and they again track the PSF position, Strehl ratio, and its intensity (see § 5).

### 3. CORONAGRAPHIC PSFs WITH ADDED PHASE/AMPLITUDE MASK

The analysis presented in § 2 was done using a far-field approximation without the use of a coronagraph. If a coronagraph is used, the amplitude/phase mask needs to be introduced before the focal plane occulter so that the satellite PSFs are replicas of the unocculted PSF. If we consider a simple pupil-plane Gaussian apodizer, it is easy to understand from equations (8) and (12) that the conclusions of § 2 are still valid for a coronagraph, since the PSFs are simply obtained with  $A$  being the apodized pupil instead of a uniform pupil. The apodized Gaussian coronagraph was chosen here, since the PSF diffraction core is still detectable and can thus be used to verify that satellite PSFs track the PSF core position and its intensity. The result would be the same for a band-limited (Kuchner & Traub 2002) or a standard Lyot coronagraph, since the grating is introduced in a pupil plane before the focal plane mask occulter and because, similarly to the apodized pupil coronagraph, these coronagraphs produce PSFs that are dominated by the second-order halo term (Perrin et al. 2003; Bloemhof 2004). A Gaussian apodized pupil for a  $1.6\ \mu\text{m}$  monochromatic PSF was simulated using the transmissive amplitude grating with and without 150 nm rms phase aberration (see Fig. 4). The pupil apodization was simulated by convolving the uniform pupil by a Gaussian having a FWHM equal to one-quarter of the pupil diameter. The simulation confirms that the satellite PSFs do again track the PSF core position and intensity.

### 4. EXPECTED ASTROMETRIC AND PHOTOMETRIC PRECISION

The aberrated PSF, the neglected terms of equations (7) and (11), and the rest of the terms in equation (6) show symmetries or antisymmetries that can, in the presence of aberrations or mask shifts, slightly affect the PSF center and intensity derived from the satellite PSFs. The task of finding the dominant terms in different regimes is complicated by the fact that  $F_a$  is complex; the imaginary and real parts of the terms in equations (7) and (11) are not necessarily, respectively, antisymmetric and symmetric, as in the unaberrated case.

For simplicity let us first consider the case without aberrations. In this case,  $F_a$  is the field strength of a perfect PSF; it is thus real and symmetric. The first neglected term of equation (7) is antisymmetric and affects the astrometric precision, and the second one is symmetric and affects the photometric precision (higher order neglected terms from the Taylor expansion have a negligible effects, since they are at least  $\Phi_{\text{mask}}$  times smaller than these two terms). The amplitudes of these terms are function of  $\Phi_{\text{mask}}$ . If  $\Phi_{\text{mask}}$  is antisymmetric, the second term is zero and the first term is maximal (astrometric error only), while if  $\Phi_{\text{mask}}$  is symmetric, the first term is zero and the second term is maximal (photometric error only). The symmetry of the mask is determined by its position in the pupil and may vary due to flexure or removal/reinsertion. The astrometric error is proportional to the ratio of

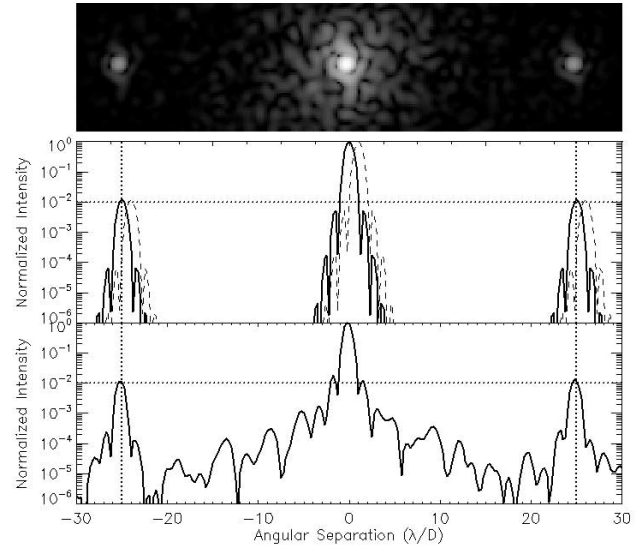


FIG. 4.—Same as Fig. 1, but for a Gaussian apodized pupil coronagraph with a transmissive amplitude grating.

the amplitude of the first neglected term to the fourth term of equation (7), or  $F_a/\Phi_{\text{mask}}$ . The photometric error is proportional to the ratio of the amplitude of the second neglected term to the fourth term, or  $F_a$ . Thus, astrometric measurements with brighter satellite PSFs are less affected by a mask offset.

For the amplitude mask without aberration, the neglected term of equation (11) produces only a symmetric structure (photometric error only). If the mask is antisymmetric, the term is zero and the satellite PSF intensity is thus equal to the expected value, while if the mask is symmetric, the term is maximal and a photometric error is present. Again, a mask offset can induce symmetry variations and cause a photometric error. The photometric precision is proportional to the ratio of the neglected term to the third term of equation (11), or  $F_a/\Phi_{\text{mask}}$ . The photometric precision is less sensitive to a mask offset when the satellite PSFs are brighter.

As mentioned previously, since  $F_a$  is complex, the case with aberrations is much more complicated. Astrometric and photometric errors can arise from both imaginary and real parts. Furthermore, the residual symmetric and antisymmetric speckle noise from the PSF will also influence the level of accuracy. Intuitively, it is expected that brighter satellite PSFs will result in a better astrometric and photometric precision.

### 5. SIMULATED PERFORMANCES

In previous sections it was shown that periodic amplitude or phase masks can be used for astrometry and photometry calibration of saturated and coronagraphic PSFs. In realistic conditions, the satellite PSFs are overlaid over a background of speckle noise that can affect the determination of the satellite PSFs centers and intensities. It is thus important to adjust the intensity of the satellites PSFs to ensure that the desired accuracy is realized. Since we have assumed that the speckle noise limits the astrometric and photometric precision, the sky background, detector read, and photon noises are neglected. Numerical simulations are now used to analyze the registering and photometric precision of the technique. Each satellite PSF is cross-correlated with a Gaussian to determine its precise location. The average  $X$  and  $Y$  positions of two symmetric satellite PSFs are then used to derive the PSF center. This derived position is then compared to the calculated PSF center using the same cross-correlation algorithm on the

TABLE 1  
ASTROMETRIC AND PHOTOMETRIC PRECISION WITH MASK OFFSET  
( $\lambda/D = 4$  PIXELS, NO ABERRATION)

Mask Type	Offset (period)	Coronagraph	$\Delta x_c$	$\Delta y_c$	$I_{\text{satel}}/I_{\text{PSF}}$
Phase .....	0	No	−0.31	0.00	0.00100
	1/4	No	0.00	0.00	0.00099
	0	Yes	0.00	0.00	0.00100
	1/4	Yes	0.00	0.00	0.00099
Amplitude.....	0	No	0.00	0.00	0.00100
	1/4	No	0.00	0.00	0.00088
	0	Yes	0.00	0.00	0.00100
	1/4	Yes	0.00	0.00	0.00100
Grating .....	0	No	0.00	0.00	0.01211
	1/4	No	0.00	0.00	0.01237
	0	Yes	0.00	0.00	0.01240
	1/4	Yes	0.00	0.00	0.01240

PSF core. Relative intensities are simply obtained by taking the ratio of the satellite’s peak intensity over that of the primary PSF. The coronagraph was simulated by simply convolving the pupil by a Gaussian having a FWHM equal to one-quarter of the pupil diameter. The brightness of the satellite PSFs was adjusted to 0.1% of the PSF peak intensity, which correspond to 100 times the background speckle noise of an aberrated (150 nm rms) non-coronagraphic PSF. Both the phase and amplitude sine phase masks are antisymmetric on the pupil, while the grating is symmetric (it is impossible to get a purely antisymmetric mask using a transmission amplitude grating). The first simulation is performed without aberration (see Table 1). As mentioned in § 4, only the phase mask shows astrometric errors when the mask is displaced, while all mask types show small photometric errors. The use of a coronagraph attenuates interference terms and yields a better astrometric and/or photometric precision in all cases.

Twenty simulations using independent 150 nm rms phase aberrations were then realized for phase sine, amplitude sine, and amplitude grating masks for cases both with and without the coronagraph. Table 2 summarizes the achievable registering and photometric precision. Typically, an astrometric error of 0.3 pixels rms ( $\sim 1/15 \lambda/D$ ) is found for both the noncoronagraph and the coronagraph cases. Typical relative intensities are precise to less than 5%, enough for accurate flux normalization.

Table 3 presents the registering and photometric accuracies for the noncoronagraph and coronagraph cases using the sine wave amplitude mask for different satellite PSF intensities relative to the local speckle noise. Satellite PSFs  $\sim 10$  times brighter than the speckle noise limit the PSF registering accuracy to 1.2 pixels rms ( $\frac{1}{3} \lambda/D$ ) and the photometric calibration to 15%–20%,

while satellite PSFs, being  $\sim 100$  times brighter than the background speckle noise, limit the PSF registering to 0.3 pixels rms ( $\sim 1/15 \lambda/D$ ) and the photometric calibration to 5%. We note that both the astrometric and photometric precision increase as the square root of the ratio of the satellite PSF intensity to the speckle noise background, i.e.,  $F_a/\Phi_{\text{mask}}$ . Since this is the dependence that was found in § 4 for the unaberrated case, it is tempting to conclude that the second term of equation (11) introduces both astrometric and photometric errors, as was expected from the fact the  $F_a$  is complex.

A satellite PSF relative intensity of  $\sim 100$  times the background speckle noise seems to be a good choice to avoid overluminous satellite PSFs, while offering good registering and photometric accuracy (0.3 pixels rms [ $\sim 1/15 \lambda/D$ ] and 5%). Such an astrometric precision (0.003 for diffraction limited *H*-band images acquired with a 10 m telescope) is sufficient to confirm proper motion of nearby systems (typically 0.01 to 0.1 yr<sup>−1</sup>) in 1 year.<sup>3</sup> Due to detector dynamic range limits, to minimize satellite PSF intensities, it might be more convenient to use a large number of fainter satellite PSFs to average the speckle noise bias, albeit at the cost of a greater field-of-view (FOV) contamination, or to choose a mask frequency to move the satellite PSFs to wide separations, where the speckle noise is generally smaller.

## 6. LABORATORY EXPERIMENT

A transmissive amplitude grating has been tested on the Université de Montréal high-contrast imaging test bed. Commercial lenses were used to make an *f*/31 imaging system, yielding, at 1.625  $\mu\text{m}$  and with a 3% filter bandpass, a PSF having 2.7 pixels per  $\lambda/D$ . The pupil diameter was 13.1 mm. A transmissive amplitude grating mask having  $150 \pm 10 \mu\text{m}$  thick wires and  $595 \pm 15 \mu\text{m}$  spacing was introduced 10 mm from the pupil plane. This slight offset was necessary due to the mask and pupil stop mounts. The geometric pupil diameter at the grating mask conjugated plane is calculated to be 12.75 mm. With this setup, the diffraction envelope of a single wire drops to 0.97 of its peak at a separation of 17.1  $\lambda/D$ , the location of the first satellite PSF pair. Neglecting the satellite PSFs chromaticity, the value is less than 0.6  $\lambda/D$ ; it is thus expected that this grating will produce satellite PSFs having a relative intensity of  $0.97 \times (150/595)^2 = 0.062 \pm 0.012$  at  $17.1 \pm 0.5 \lambda/D$  separation. The pinhole was moved and

<sup>3</sup> For speckle noise–limited companion detections, the derived astrometric precision from § 5 simulations also mean that companions need to be at least 100 times brighter than the background speckle noise to obtain 1/15  $\lambda/D$  center determination accuracy and allow their proper-motion follow-up in 1 year for typical nearby systems. Fainter companions will require a bigger time interval or longer integration time, assuming that the object S/N is increasing with integration time.

TABLE 2  
SIMULATED ASTROMETRIC AND PHOTOMETRIC PRECISION ( $\lambda/D = 4$  PIXELS)

Aberration	Coronagraph	With 150 nm rms	$\Delta X_C$ rms (pixel)	$\Delta Y_C$ rms (pixel)	$I_{\text{satel}}/I_{\text{PSF}}$	$I_{\text{satel}}/I_{\text{PSF}}$ rms (%)	$I_{\text{satel}}/I_{\text{PSF}}$ Expected
Phase .....	No	No	...	...	0.00100	...	0.00100
	No	Yes	0.19	0.18	0.00100	0.00001 (1.0)	0.00100
	Yes	Yes	0.15	0.10	0.00099	0.00001 (1.0)	0.00100
Amplitude.....	No	No	...	...	0.00100	...	0.00100
	No	Yes	0.24	0.20	0.00102	0.00005 (5)	0.00100
	Yes	Yes	0.19	0.18	0.00103	0.00005 (5)	0.00100
Grid .....	No	No	...	...	0.01240	...	0.01235
	No	Yes	0.12	0.15	0.01198	0.00010 (0.8)	0.01235
	Yes	Yes	0.05	0.03	0.01235	0.00010 (0.8)	0.01235

TABLE 3  
SATELLITE PSF INTENSITY VERSUS ASTROMETRIC AND PHOTOMETRIC PRECISION ( $\lambda/D = 4$  PIXELS)

Satellite PSF Intensity to Speckle Noise Ratio <sup>a</sup>	Coronagraph	$\Delta X$ rms	$\Delta Y$ rms	$I_{\text{satel}}/I_{\text{PSF}}$	$I_{\text{satel}}/I_{\text{PSF}}$ rms (%)
10.....	No	0.78	0.93	0.00013	0.00002 (15)
16.....	Yes	0.75	0.80	0.00011	0.00002 (18)
100.....	No	0.24	0.20	0.00102	0.00005 (5)
160.....	Yes	0.19	0.18	0.00103	0.00005 (5)
1000.....	No	0.07	0.06	0.01003	0.00018 (1.8)
1600.....	Yes	0.06	0.05	0.01005	0.00014 (1.4)
10,000.....	No	0.02	0.02	0.10214	0.00092 (0.9)
16,000.....	Yes	0.02	0.02	0.10156	0.00067 (0.7)

<sup>a</sup> In all cases, satellite PSF intensities are 0.1% fainter than the PSF peak intensity. The satellite PSF intensity to speckle noise ratios are higher when using a coronagraph, since, for these cases, the speckle noise is attenuated by the coronagraph by a factor 1.6 in our simulations.

an aberration phase plate was introduced in the beam, producing a Strehl ratio 25% lower, to confirm that these satellite PSFs do track the PSF core position and intensity. All acquired images were unsaturated and reduced by subtracting a dark frame and dividing by a flat field. The two brightest satellite PSFs are 160 times brighter than the background noise. Figure 5 shows the resulting PSFs. Satellite PSFs have a relative intensity of 0.058 and are situated at  $16.9 \lambda/D$  from the PSF center, both values being consistent with the calculated values to  $1 \sigma$  accuracy, and they track the PSF core position and its intensity, in agreement with what was expected. In all of these experiments, it was possible to register the PSF to less than 0.1 pixel precision ( $1/30 \lambda/D$ ) with the average position of two symmetric satellite PSFs, and the relative intensities are constant to several percent (see Table 4), all consistent with the expected accuracy for satellite PSFs that are 100–1000 times the background noise (see Table 3).

## 7. ON-SKY IMPLEMENTATION

If we consider the Gemini Altair AO system (Herriot et al. 1998) and the Near-IR Imager (NIRI; Hodapp et al. 2000) for a possible implementation, satellite PSFs  $\sim 10$  mag fainter than the central peak should be  $\sim 100$  times brighter than the speckle noise at  $4''$  (Marois et al. 2006). If we put a transmission amplitude

grating just in front of Altair's deformable mirror, where the wave front diameter is 84 mm, a wire spacing and thickness of 2 mm and  $18 \mu\text{m}$ , respectively, would be required to produce satellite PSFs 10 mag fainter at  $1''$  intervals. Such a configuration has 99.1% transmission (see Fig. 6 for a simulated example).

For high-contrast imaging attempting to achieve detection limits of the order of 20 mag at less than  $1''$ , e.g., the Gemini Planet Imager (GPI) and the VLT Planet Finder (VLTPF) projects, wire thickness will become an issue. A potential solution is to increase the wire spacing to place the satellite PSFs at  $5 \lambda/D$ . Using the same  $18 \mu\text{m}$  thick wires and a wave front diameter as in the above example, would produce satellite PSFs that are 15 mag fainter than the primary. For more advanced coronagraphic projects aiming for Earth-like exoplanet detections at 24 mag contrast, a simple approach is to put the wires directly on the primary mirror. A series of 10  $18 \mu\text{m}$  thick wires across an 8 m diameter telescope will produce satellite PSFs 23.2 mag fainter than the primary at  $10 \lambda/D$  (99.998% transmission).

Another solution is to generate satellite PSFs using a small periodic phase aberration. In a conventional AO system with a separate wave front sensor this could be achieved by adding a sinusoidal offset to the control point that the wave front sensor attempts to achieve. Most AO systems operate with their wave front control loop seeking not a flat wave front in the sensor but a wave front offset by the conjugate of any non-common-path aberrations between the wave front sensor and science channel. Adding an additional sinusoidal component to this offset would result in a time-averaged PSF containing the satellite PSFs. As long as the sinusoid is lower in amplitude than the typical residual wave front, 200–300 nm for current AO systems (van Dam & Macintosh 2003) and 50–100 nm for extreme AO (Macintosh et al. 2004; Mouillet et al. 2004), and the wave front sensor is operating in a linear regime, this should have little effect on other components of the image. For systems without a separate wave front sensor—e.g., the Terrestrial Planet Finder Coronagraph, which is intended to use science-camera images on a reference target to control the deformable mirror via iterative phase diversity, the satellite images could be built into the target wave front or focal-plane image that the phase diversity image sequence converges to. The satellite PSFs can then be used to estimate the PSF changes between the reference and science targets.

## 8. DISCUSSION

The simulations presented in this paper are monochromatic. For bandpasses of finite size, off-axis satellite PSFs will be elongated and thus fainter relative to the core. The satellite PSF

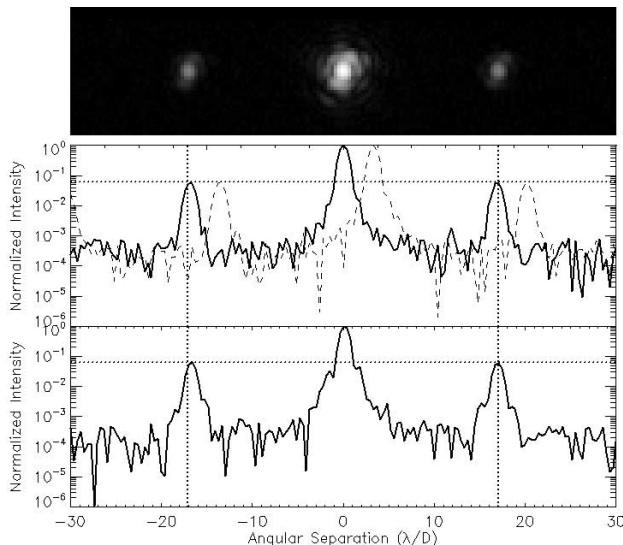


FIG. 5.—Same as Fig. 1, but for the laboratory experiment using a transmissive amplitude grating.

TABLE 4  
LABORATORY EXPERIMENT

PSF Type	PSF		SATELLITE PSFs		$\Delta XC$	$\Delta YC$	$\langle I_{\text{satel}}/I_{\text{PSF}} \rangle$
	$XC$	$YC$	$XC$	$YC$			
Unaberrated .....	199.93	199.98	199.90	200.05	0.03	−0.07	0.055
Aberrated .....	200.08	199.69	199.99	199.68	0.09	0.01	0.061
Shifted .....	200.45	209.04	200.45	209.07	0.00	−0.03	0.059

elongation is simply proportional to the filter bandpass  $\Delta\lambda/\lambda$  times the satellite PSF angular separation. In addition, for ground-based imaging, if no atmospheric dispersion corrector is used, the elongation of the satellite PSFs will not necessarily point toward the PSF center due to differential atmospheric refraction between the blue and red side of the bandpass (Filippenko 1982; Roe 2002). For  $H$ -band observations within  $\pm 2$  HA, the amplitude of this effect can be several tens of milliarcseconds, i.e., of the order of  $1 \lambda/D$ , as observed by precise registration of two near-infrared narrowband PSFs made with the TRIDENT camera at the Canada-France-Hawaii Telescope (CFHT; Marois et al. 2005). However, satellite PSF chromaticity and differential atmospheric refraction do not influence the astrometry precision, since the midpoint of the line connecting the centers of opposite satellite PSFs still coincides with the PSF center. For large bandpasses and/or satellite PSFs at large angular separations, the satellite PSF photometry can be partially correlated with a Strehl ratio variation, since the required aperture necessary to estimate the satellite PSF intensity will need to be larger than a  $\lambda/D$  diameter; it would thus be better to choose a satellite PSF at small separation to minimize this effect.

Distortions coming from optics after the added mask can change the relative position of the satellite PSFs. The satellite PSF position will thus need to be calibrated using an internal source or on-sky observations. To obtain precise relative astrometry of detected companions, distortion corrections for the entire optical system is also required. For ground-based imaging, two effects are potentially not correctable with the satellite PSF technique. If a wide bandpass is used, spectral differences between the companion and the primary coupled with differential atmospheric refraction can

introduce small astrometric errors as a function of air mass. This effect is negligible for Integral Field Units (IFUs) or narrowband imaging and can, for cases when it is important, be accounted for by analysis the companion spectrum. Anisoplanatism variations can also degrade the companion Strehl ratio without affecting that of the primary, thus possibly introducing companion photometric errors. Since high-contrast imaging projects usually have small FOV (several arcseconds wide) compared to a standard AO anisoplanatism angle ( $\sim 30''$  radius), such an effect is relatively small.

The satellite PSFs will occupy a small portion of the FOV. Once the PSF is registered and flux normalized, the satellite PSFs could be removed to avoid masking faint sources. Since the angular separation and size of the satellite PSFs are chromatic and fixed with respect to the instrument, a simple way to remove them while conserving the flux of nearby sources would be to use the simultaneous spectral differential imaging (SSDI; Racine et al. 1999; Marois et al. 2000, 2005; Sparks & Ford 2002; Biller et al. 2004) and/or angular differential imaging (ADI) techniques (Marois 2004; Liu 2004; Marois et al. 2006). If these techniques still leave important localized residuals, the satellite PSFs can simply be masked.

## 9. CONCLUSION

It is shown both analytically and numerically that periodic amplitude and phase masks conjugated to the pupil plane with and without a coronagraph can be used to produce satellite PSFs that track the PSF core position and its intensity. The astrometric and photometric precision is proportional to the square root of the ratio of the satellite PSF intensity to the background speckle noise. Satellite PSFs 100 times brighter than the speckle noise achieve a registering and photometric accuracy of 0.3 pixels rms ( $\sim 1/15 \lambda/D$ ) and 5%, respectively. Such precision is sufficient to properly combine images and to confirm the proper motion of nearby systems within 1 yr with AO on a 10 m telescope.

As illustrated by the laboratory experiment, this technique can be easily implemented by using a transmissive amplitude grating. The experiment confirms that an amplitude mask conjugated to the pupil plane produces such satellite PSFs and that they track the PSF core position and intensity, while demonstrating the simplicity of the method.

This technique could play an important role in current AO systems and next-generation extreme AO coronagraph systems such as the Gemini Planet Imager (Macintosh et al. 2004, 2006) or the VLT Planet Finder (Mouillet et al. 2004), as well as in future high-contrast coronagraphic space observatories.

The authors would like to thank Anand Sivaramakrishnan for stimulating discussions. This research was performed under the

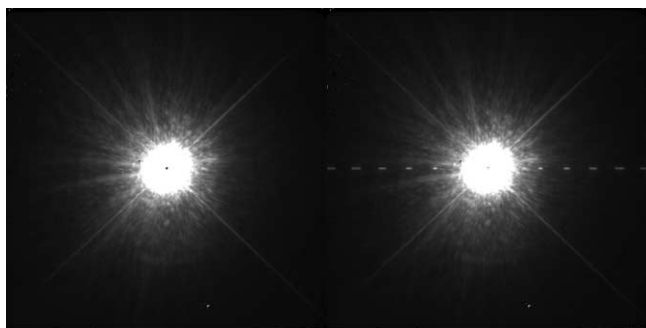


FIG. 6.—Observed 30 s  $\text{CH}_4$ -band Gemini Altair/NIRI saturated PSF (left; star has  $m_H = 5$ ) and with simulated satellite PSFs (right). Simulated satellite PSFs are for a series of 42 wires having  $18 \mu\text{m}$  thickness across a 84 mm pupil. Satellite PSFs are  $\sim 10$  mag fainter than the primary and are located at  $\sim 1.7''$  intervals along the  $x$ -axis. They are produced using nonsaturated data acquired in the same filter and normalized to the same integration time as the saturated image. Satellite PSFs have approximately the same intensity contrast in the FOV, since the sinc modulation FWHM from the wire thickness (see eq. [13]) is  $\sim 9$  times the FOV (FOV is  $22.4'' \times 22.4''$ ). The satellite PSF elongation is simulated for the filter 6.5% bandpass. The PSF is saturated inside  $0.8''$  radius.

auspices of the Department of Energy by the University of California, Lawrence Livermore National Laboratory, under contract W-7405-ENG-48, and was also supported in part by the National Science Foundation Science and Technology Center for Adaptive Optics, managed by the University of California at Santa

Cruz under cooperative agreement AST 98-76783. This work is supported in part through grants from the Natural Sciences and Engineering Research Council, Canada, and from the Fonds Québécois de la Recherche sur la Nature et les Technologies, Québec.

## REFERENCES

- Biller, B. A., Close, L., Lenzen, R., Brandner, W., McCarthy, D., Nielsen, E., & Hartung, M. 2004, *Proc. SPIE*, 5490, 389
- Bloemhof, E. E. 2004, *ApJ*, 610, L69
- Bloemhof, E. E., Dekany, R. G., Troy, M., & Oppenheimer, B. R. 2001, *ApJ*, 558, L71
- Filippenko, A. V. 1982, *PASP*, 94, 715
- Hecht, E. 1998, *Optics* (3rd ed.; Reading: Addison Wesley Longman)
- Herriot, G., Morris, S., Roberts, S., Fletcher, J. M., Saddlemeyer, L. K., Singh, G., Veran, J., & Richardson, E. H. 1998, *Proc. SPIE*, 3353, 488
- Hodapp, K., Hora, J., Graves, E., Irwin, E. M., Yamada, H., Douglass, J. W., Young, T. T., & Robertson, L. 2000, *Proc. SPIE*, 4008, 1334
- Kuchner, M. J., & Traub, W. A. 2002, *ApJ*, 570, 900
- Liu, M. C. 2004, *Science*, 305, 1442
- Lyot, B. 1932, *Z. Astrophys.*, 5, 73
- Macintosh, B., et al. 2004, *Proc. SPIE*, 5490, 359
- . 2006, *Proc. SPIE*, 6113, 08
- Marois, C. 2004, Ph.D. thesis, Univ. Montréal
- Marois, C., Doyon, R., Racine, R., & Nadeau, D. 2000, *PASP*, 112, 91
- Marois, C., Doyon, R., Racine, R., Nadeau, D., Riopel, M., Vallée, P., & Lafrenière, D. 2005, *PASP*, 117, 745
- Marois, C., Lafrenière, D., Doyon, R., & Nadeau, D. 2006, *ApJ*, 641, 556
- Mouillet, D., Lagrange, A. M., Beuzit, J.-L., Moutou, C., Saisse, M., Ferrari, M., Fusco, T., & Boccaletti, A. 2004, in *ASP Conf. Ser. 321, Extrasolar Planets: Today and Tomorrow*, ed. J.-P. Beaulieu, A. Lecavelier des Etangs, & C. Terquem (San Francisco: ASP), 39
- Perrin, M. D., Sivaramakrishnan, A., Makidon, R. B., Oppenheimer, B. R., & Graham, J. R. 2003, *ApJ*, 596, 702
- Racine, R., Walker, G. A. H., Nadeau, D., Doyon, R., & Marois, C. 1999, *PASP*, 111, 587
- Roe, H. G. 2002, *PASP*, 114, 450
- Schroeder, D. J. 1987, *Astronomical Optics* (San Diego: Academic Press)
- Sivaramakrishnan, A., Lloyd, J. P., Hodge, P. E., & Macintosh, B. A. 2002, *ApJ*, 581, L59
- Sivaramakrishnan, A., & Oppenheimer, B. 2006, *ApJ*, 647, 620
- Sparks, W. B., & Ford, H. C. 2002, *ApJ*, 578, 543
- van Dam, M. A., & Macintosh, B. A. 2003, *Proc. SPIE*, 5169, 1